

Geophysical Research Letters

RESEARCH LETTER

10.1029/2021GL093679

Key Points:

- A weak layer or zone beneath the spinel-to-post-spinel phase transition leads to deflected slab structures in the mantle transition zone
- Trench retreat velocity and the viscosity contrast between the upper and the lower mantle also affect horizontally deflected slab formation
- The weak zone is controlled by the grain size reduction following the phase transition and subsequent grain growth rate

Supporting Information:

Supporting Information may be found in the online version of this article.

Correspondence to:

W. Mao and S. Zhong,
wei.mao@colorado.edu;
shijie.zhong@colorado.edu

Citation:

Mao, W., & Zhong, S. (2021). Formation of horizontally deflected slabs in the mantle transition zone caused by spinel-to-post-spinel phase transition, its associated grain size reduction effects, and trench retreat. *Geophysical Research Letters*, 48, e2021GL093679. <https://doi.org/10.1029/2021GL093679>

Received 1 APR 2021

Accepted 5 JUL 2021

Formation of Horizontally Deflected Slabs in the Mantle Transition Zone Caused by Spinel-to-Post-Spinel Phase Transition, Its Associated Grain Size Reduction Effects, and Trench Retreat

Wei Mao¹  and Shijie Zhong¹ 

¹Department of Physics, University of Colorado, Boulder, CO, USA

Abstract Seismic observations indicate accumulation of subducted slabs in the mantle transition zone in many subduction zones. By systematically conducting 2-D numerical experiments, we demonstrate that a weak layer or zone beneath the spinel-to-post-spinel phase transition leads to horizontally deflected (stagnant) slab structures in the mantle transition zone, which is consistent with recent studies of 3-D global mantle convection models. Trench retreat velocity, Clapeyron slope and the viscosity contrast between the lower mantle and mantle transition zone also affect horizontally deflected slab formation. By considering grain size dependent viscosity and grain size evolution for slabs going through the phase change in the lower mantle, our models with a dynamically generated weak zone beneath the phase boundary indicate that the geometry and viscosity reduction of the weak zone is strongly affected by grain growth rate. A smaller grain growth rate results in a thicker and wider weak zone that promotes deflected slab formation.

Plain Language Summary When oceanic plates subduct into the deep mantle, some of them penetrate from the upper mantle to the lower mantle directly, others are horizontally deflected over a long distance in the mantle transition zone above 670-km depth as indicated by recent seismic observations. In this study, by conducting numerical experiments, we demonstrate that this phenomenon could be explained by presence of a weak layer or zone in the lower mantle immediately beneath the mantle transition zone. The weak zone is generated due to grain size reduction after phase change of mantle minerals. By considering grain size dependent viscosity and grain size evolution for subducted slabs going through the phase change in the lower mantle, our models with a dynamically generated weak zone beneath the phase boundary indicate that the geometry and viscosity reduction of the weak zone is strongly affected by the grain growth rate. Our results also show that trench retreat velocity, phase change properties and the viscosity contrast between the lower mantle and mantle transition zone also affect the horizontally deflected slab formation.

1. Introduction

Seismic observations reveal distinctly different morphologies of subducted slabs in the mantle transition zone (Goes et al., 2017). At some subduction zones (e.g., the North America and the Central America), slabs penetrate into the lower mantle and could reach the core-mantle-boundary (e.g., Grand et al., 1997; van der Hilst et al., 1997); while at other subduction zones (e.g., in the Honshu, Bonin, and Chile), slabs appear to be deflected and extend horizontally over a long distance in the mantle transition zone above the 670 km depth (French & Romanowicz, 2014, 2015; Fukao & Obayashi, 2013; Ritsema et al., 2011) (note that the horizontally deflected slabs are sometimes referred to as “stagnant” slabs in literature, although the slabs are not stationary in the mantle transition zone). Various factors affect subduction zone dynamics and contribute to the formation of deflected slabs in the mantle transition zone including trench retreat, viscosity jump from the mantle transition zone to the lower mantle, the endothermic phase change of spinel-to-post-spinel at ~670 km depth, slab age and rheology, and nonequilibrium pyroxene garnet transition (e.g., Agrusta et al., 2017; Christensen, 1996; Garel et al., 2014; Goes et al., 2017; Holt et al., 2015; King et al., 2015; Lee & King, 2011; Stegman et al., 2006; Wang & Li, 2020; Yang et al., 2018; Zhong & Gurnis, 1995). However, the relative importance of each factor is still in debate (Goes et al., 2017).

Previous 2-D modeling studies suggest the requirement of a large Clapeyron slope of the spinel-to-post-spinel phase transition (≥ 3.0 MPa/K) to explain deflected slab (e.g., Yang et al., 2018; Zhong & Gurnis, 1995), which is inconsistent with a relatively low value of ~ 1.3 – 2.5 MPa/K inferred from mineral physics (Fei et al., 2004; Katsura et al., 2003; Litasov et al., 2005) and seismic models (Fukao & Obayashi, 2013). Recently, Mao and Zhong (2018, 2019) resolved this dilemma by introducing a weak layer beneath the spinel-to-post-spinel phase transition into their 3-D global mantle convection models with imposed surface plate motion history that would lead to diverse slab structures in the mantle transition zone, including the deflected slabs structures in the western Pacific and penetrated slabs in the North and Central Americas. Mao and Zhong (2018) attributed this weak layer to the effect of grainsize reduction and super-plasticity associated with the phase change as the slabs go into the lower mantle, as previously suggested in different contexts (Karato, 2008; Mitrovica & Forte, 2004; Panasyuk & Hager, 1988; Solomatov & Reese, 2008). Recently, Mao and Zhong (2021) found that the weak layer only needs to exist in subduction zones (i.e., no need to be a global layer) to reproduce the seismically observed deflected slabs. In addition, the convection models show significant correlations with seismic tomographic models up to spherical harmonic degree 20 in the upper mantle and mantle transition zone (Mao & Zhong, 2019; Rudolph et al., 2020).

Grain size dependent viscosity may strongly influence the dynamics of plate tectonics, mantle convection and thermal evolution of the Earth (e.g., Behn et al., 2009; Bellas et al., 2018; Bercovici et al., 2019; Čížková et al., 2002; Dannberg et al., 2017; Hall & Parmentier, 2003; Korenaga, 2005; Panasyuk & Hager, 1998; Rozel, 2012; Solomatov, 2001; Solomatov & Reese, 2008; Thielmann & Schmalholz, 2020). The spinel-to-post-spinel phase transition could lead to significant grainsize reduction (i.e., from a few centimeters to micrometers [e.g., Solomatov & Reese, 2008; Yamazaki et al., 1996, 2009]), thus resulting a weak layer beneath the mantle transition zone (e.g., Fei et al., 2021; Panasyuk & Hager, 1998). However, the grainsize, its evolution in the mantle and its effect on mantle viscosity remain poorly understood largely because of the lack of observational constraints (Glišović et al., 2015; Solomatov & Reese, 2008). Therefore, the proposal by Mao and Zhong (2018) that seismically observed deflected slabs may result from grainsize reduction following phase change may provide a potentially important observational constraint on grainsize effect on mantle viscosity.

However, there are a number of shortcomings and issues on the studies of the effects of the weak layer on the deflected slabs. With their 3-D global convection models with realistic plate motion history, Mao and Zhong (2018, 2021) were unable to explore systematically a large enough parameter space on the effects of the weak layer. Grain size dependent viscosity and grainsize evolution were not implemented in models of Mao and Zhong (2018, 2021) where the weak layer was defined either as a global layer or by temperature of slabs. Additionally, although both 2-D regional models (Grima et al., 2020) and 3-D global models with imposed plate motion history show consistent results on the effects of the weak layer on deflected slabs (Lourenço & Rudolph, 2020; Mao & Zhong, 2018), the effects may appear to be different in some 2-D models (Li et al., 2019). To address these issues, here we formulate 2-D model calculation with grain size dependent viscosity and grainsize evolution to examine the formation of the weak layer beneath the spinel-to-post-spinel phase change and their effects on the dynamics of the slabs.

2. Methods and Model Setup

We use the 2-D Cartesian mantle convection code Citcom (Moresi & Gurnis, 1996; Moresi et al., 1996) to solve the governing equations of the conservation of mass, momentum and energy (see Supporting Information S1 for details). Our models with prescribed kinematic surface boundary conditions to control trench retreat are similar to Christensen (1996) that also investigated the dynamics of deflected slabs above the 670 km depth. We use a mesh with 401 horizontal and 161 vertical grid points and refined mesh near the surface, subduction zone and phase transition zone so that in these regions the resolution reaches 10×10 km. For most cases, the total model time is over 50 Myr, allowing sufficient slab evolution. Mantle viscosity in our models is generally depth, and temperature, and grain size dependent and the nondimensional form is

$$\eta(T, r, c) = \eta_r(r) c^p \exp[E(0.5 - T)] \quad (1)$$

where $\eta_r(r)$ is the depth-dependent prefactor, E is the nondimensional activation energy, c is the grain size, and p is the grainsize exponent which is set to be 3 (e.g., Solomatov & Reese, 2008), except for cases with no grainsize effect for which $p = 0$.

Most models in this study include a weak layer below the phase change boundary, as in Mao and Zhong (2018, 2019). For models with a global weak layer as in Mao and Zhong (2018), this weak layer is defined using phase function Γ (see Supporting Information S1). For $\Gamma < 0.5$, the mantle viscosity is the same as that in the transition zone. However, for $0.5 < \Gamma < 0.99$, the mantle is considered in superplastic post-spinel phase, and its viscosity pre-factor is reduced to be 1/10 of the transition zone value. The effective thickness of the weak layer is ~ 60 km. For $\Gamma > 0.99$ (i.e., the lower mantle), the normal post-spinel phase viscosity is applied.

The weak layer might only exist beneath subducted slabs as a result of the spinel-to-post-spinel phase change (e.g., Panasyuk & Hager, 1998; Solomatov & Reese, 2008). Therefore, we also consider a regional weak layer model in which the weak layer is confined beneath slabs using the temperature criteria as in Mao and Zhong (2021)

$$\delta T = T - T_{\text{ave}} < -0.01 \quad (2)$$

where δT and T_{ave} are the nondimensional temperature anomaly and horizontally averaged temperature, respectively.

We also further test models with a dynamically generated weak layer by considering grain size dependent viscosity and grainsize evolution. For simplicity, using a similar formulation to that in Solomatov and Reese (2008), we only consider grainsize reduction following the spinel-to-post-spinel phase transition and its subsequent grainsize evolution in the lower mantle. The initial dimensionless grain size c is set to be 1.0 (dimensional value of 200 μm) for the whole mantle and 16 tracers in each element are used to track the grainsize evolution. Tracer movement is implemented as in thermochemical convection models (McNamara & Zhong, 2004). For each tracer, we calculate both the phase function Γ and grain size c at each time step. Once the phase function Γ of a tracer changes to ≥ 0.5 at a new step, which suggests the occurrence of spinel-to-post-spinel phase transition, the grainsize is reduced to c_{ph} . For tracers which have experienced grainsize reduction following the phase change into the lower mantle, the nondimensional grainsize starts to grow at a rate (e.g., Solomatov & Reese, 2008):

$$G = \frac{Dc}{Dt} = Kc^{1-m} \exp\left[-\theta_g \left(\frac{1}{T'_0 + T} - \frac{1}{T'_0 + 1}\right)\right] \cong Kc^{1-m} \exp[-\theta_g(1 - T)] \quad (3)$$

where $T'_0 = \frac{T_0}{\Delta T}$, m , K , and θ_g are the normalized surface temperature with T_0 as the surface temperature of 273 K, grain growth exponent, grain growth pre-exponent factor and the Frank-Kamenetskii parameter for Ostwald ripening, respectively (Table S1). m is set to be 3 or 5.2. $\theta_g = \frac{Q_g \Delta T}{RT_{\text{CMB}}^2}$ is set to 9.21, in which Q_g is the activation enthalpy for Ostwald ripening. We vary K to control grain growth rate. Given that the grain growth rate is proportional to c^{1-m} , grainsize c grows significantly slower for larger c (Figures S1 and S2). The grainsize of the ambient lower mantle is significantly larger than that of the cold slab that just experiences the phase change, it should be relatively stable over the modeling time duration of ~ 50 Myr (Fei et al., 2021; Figures S1 and S2). Therefore, we ignore grain growth of the ambient lower mantle by setting the upper limit for the grainsize c to be 1 so that we can focus on the grainsize evolution related to subducted slab.

3. Results

3.1. Effects of Weak Layer Beneath the Spinel-to-Post-Spinel Phase Transition

We first present our reference model Case 1 with Clapeyron slope (γ_{670}) of -2.0 MPa/K, trench retreat velocity (V_{tr}) of 3 cm/year, and a global weak layer beneath the phase transition (Table S2). Note that $\gamma_{670} = -2.0$ MPa/K is consistent with the experimental studies and is the same as that used in Mao and Zhong (2018). The model shows that once the slab subducts to the bottom of the mantle transition zone, it buckles above the bottom of the mantle transition zone. Then the slab spreads horizontally in the mantle

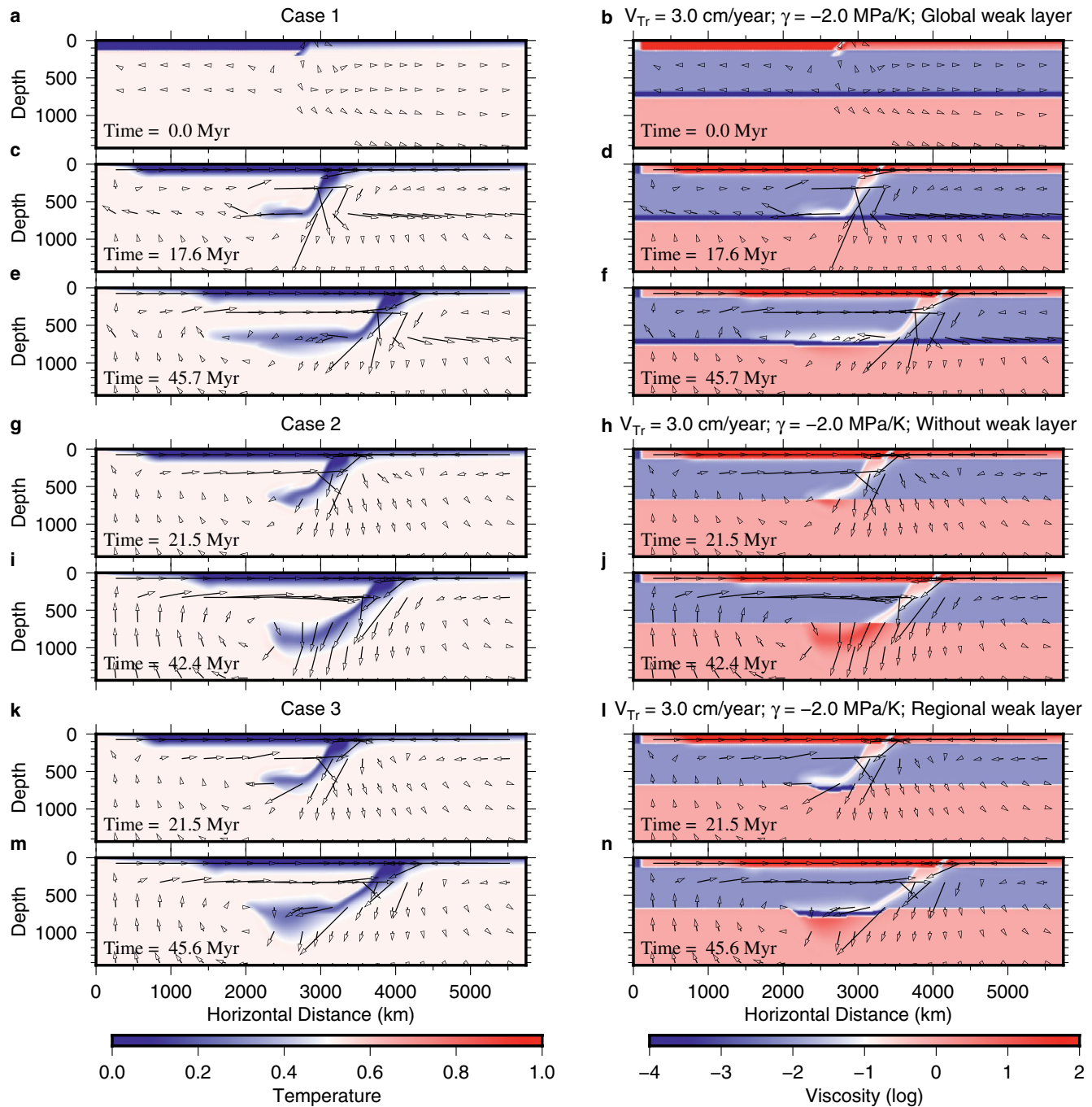


Figure 1. Snapshots of dimensionless temperature and viscosity fields for Case 1 with a global weak layer (a–f), Case 2 without weak layer (g–j), and Case 3 with a regional weak layer (k–n), respectively.

transition zone at a rate that is similar to the convergence velocity at the surface. And the horizontal distance of the deflected slab increases from ~ 700 km at 17.6 Myr (Figures 1c and 1d and Figure S3b) to $\sim 2,200$ km at 45.7 Myr (Figures 1e and 1f and Figure S3b).

We then present Case 2 that is identical to Case 1 except without the weak layer. Although the subducted slab also buckles in the mantle transition zone, it does not spread horizontally but penetrates into the lower mantle at 21.5 Myr (Figures 1g and 1h and Figure S3a). The slab keeps sinking into the lower mantle and become thicker due to larger viscosity in the lower mantle (Figures 1i–1j).

Cases 1 and 2 show the dramatic effect of the weak layer on the formation of deflected slabs in the mantle transition zone, confirming the 3-D global convection models by Mao and Zhong (2018, 2019). Panasyuk and Hager (1998) and Solomatov and Reese (2008) suggested that the viscosity reduction due to grain size reduction and superplasticity occur mainly within slabs where the radial flow velocity is large. Therefore, we formulated Case 3 to test the effects of a regional weak layer in the slab. Case 3 is identical to Case 1 except for that the weak layer is confined beneath the slab based on temperature (i.e., Equation 2). The evolution of slab morphology in Case 3 is similar to that in Case 1 (Figures 1k–1l) except the horizontal distance of deflected slab in the mantle transition zone is ~ 600 km shorter than that in Case 1 at ~ 46 Myr (Figures 1m–1n, 1e–1f and Figure S3b).

3.2. Effects of Trench Retreat and Clapeyron Slope

Both trench retreat velocity and the Clapeyron slope of the spinel-to-post-spinel phase transition have been well recognized as two most dominant parameters which contribute to deflected slab in the mantle transition zone (Christensen, 1996; Zhong & Gurnis, 1995). Case 4 is identical to Case 2 except that the trench retreat velocity is increased to 5.0 cm/year from 3.0 cm/year in Case 2. Contrary to Case 2 in which the slab descends into the lower mantle at a velocity that is similar to convergence velocity (Figures 1g–1j), Case 4 with faster trench retreat velocity results in significantly smaller sinking velocity for the slab in the mantle transition zone (Figures 2a and 2b) and the slab is deflected in the mantle transition zone over 1,500 km distance. Case 5 is identical to Case 2 except that the Clapeyron slope of the spinel-to-post-spinel phase transition is -3.5 MPa/K instead of -2.0 MPa/K. Case 5 with larger Clapeyron slope also shows a larger horizontal length of deflected slab as expected (Figures 2c–2d), compared with Case 2. The horizontal length of the deflected slab in Case 5 is slightly shorter than that in Case 1 at the similar time (~ 46 Myr) with a global weak layer and smaller Clapeyron slope of -2 MPa/K (Figures 1e–1f).

More experiments for the three different kinds of models: with a global (Figure S4a), with a regional (Figure S4b) and without the weak layer (Figure S4c), are further explored by varying the trench retreat velocity and Clapeyron slope. For models without weak layer (Figure S4c), deflected slab can only be produced when both V_{Tr} and γ_{670} are large, for example, V_{Tr} should reach 5 cm/year when γ_{670} is -2.0 MPa/K, which is consistent with previous 2-D studies (e.g., Christensen, 1996; Yang et al., 2018; Zhong & Gurnis, 1995). As a reference, in northern Honshu subduction where $\sim 1,500$ km long deflected slab is imaged seismically, the trench retreat rate is less than ~ 2 cm/year for the last 20 Myr (e.g., Seton et al., 2012) during which the deflected slab may have been formed (Mao & Zhong, 2018). For models with either a global or regional weak layer (Figures S4a and S4b), a large length deflected slab can be generated at a trench retreat velocity of 2.0 cm/year or larger when γ_{670} is -2.0 MPa/K. Interestingly, for models with a global weak layer, large length deflected slab can form even without trench retreat when γ_{670} is -2.0 MPa/K (Figure S4a).

3.3. Effects of Viscosity Jump From the Upper Mantle to the Lower Mantle

The viscosity in the lower mantle is higher than that in the mantle transition zone, which provides resistance for the slab penetration into the lower mantle. To explore its effects with the existence of a weak layer, we performed another series of model calculations with different viscosity ratios β between the lower mantle and the upper mantle. Cases 6–8 are identical to Case 1 (i.e., with a global weak layer), except that their β are 10, 30, and 60, respectively, instead of 100 (Table S2). For Cases 6 and 7 with β are 10 and 30, although initially the slab is deflected and stays horizontally above the lower mantle over a length of $\sim 1,000$ km, the tip of the slab still penetrates into the lower mantle (e.g., Figures 2e–2f for Case 7 with $\beta = 30$ at 31.0 Myr) because of small resistance. As the trench retreats, the horizontal length of the slab in the mantle transition zone decreases, and the leading part of the slab keeps sinking into the lower mantle (e.g., Figures 2g–2h for Case 7 with $\beta = 30$ at 45.2 Myr). Case 8 with $\beta = 60$ is nearly identical to Case 1 and produces a long deflected slab in the transition zone.

3.4. Effects of Slab Strength

Slab strength strongly affects slab dynamics, but it is still poorly constrained (Billen et al., 2003; Billen & Hirth, 2007; Moresi & Gurnis, 1996; Zhong & Davies, 1999). Here we vary slab viscosity by varying the

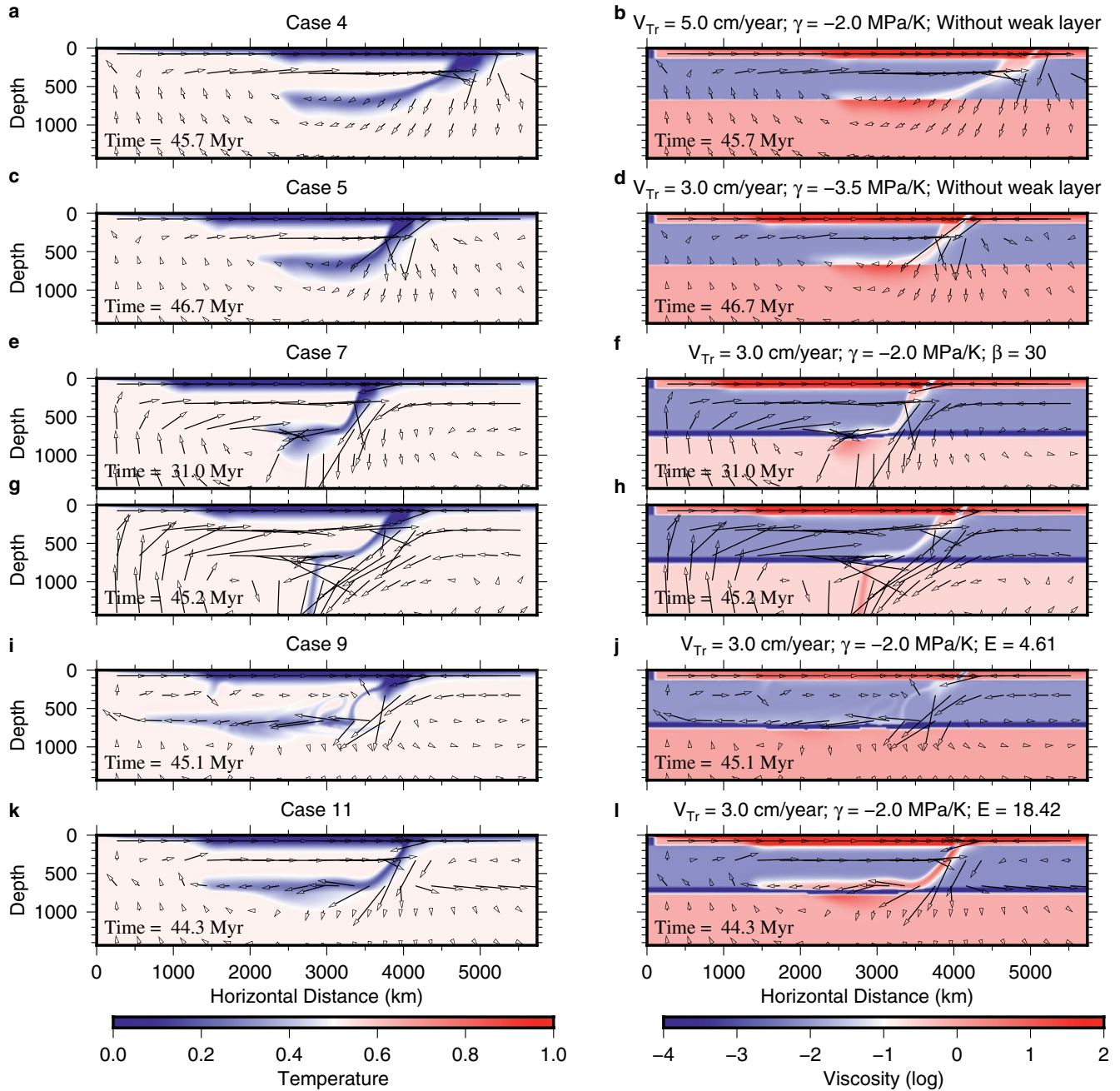


Figure 2. Snapshots of dimensionless temperature and viscosity fields for Case 4 without weak layer and $V_{Tr} = 5$ cm/year (a–b), Case 5 without weak layer and $\gamma_{670} = -3.5$ MPa/K (c–d), Case 7 with a global weak layer and $\beta = 30$ (e–h), Cases 9 and 11 with a global weak layer and $E = 4.61$ and 18.42 (i–j and k–l), respectively.

activation energy E , while fixing the ambient mantle viscosity. Cases 9, 10, and 11 (Table S2) are identical to Case 1 except their E are 4.61, 13.82, and 18.42 instead of 9.21, resulting in a total viscosity contrast of 10^2 , 10^6 , and 10^8 , respectively. Case 9 with $E = 4.61$ results in significantly faster slab sinking velocity and thinner slab in the upper mantle (Figures 2i–2j) compared with Case 1 (Figures 1c–1f). Additionally, the horizontal length of the deflected slab in the mantle transition zone is significantly larger as the slab moves faster (Figure S3b). Cases 10 and 11 with higher slab viscosity show similar long deflected slab in the mantle transition (e.g., Figures 2k–2l for Case 11 with $E = 18.42$ at 44.3 Myr) to that in Case 1.

3.5. Grain Size Dependent Viscosity

We now present models with the grain size dependent viscosity as described in Section 2. Cases 12 and 13 are identical to Case 1 except that the grain size dependent viscosity is included and the global weak layer is removed. Dimensionless grain growth pre-exponent K for Cases 12 and 13 are 10^3 and 10^5 , respectively, while the grainsize reduction factor is 30 and the grain growth exponent m is 3 for both cases. Case 12 with smaller grain growth rate shows similar slab evolution, including long deflected slab in the mantle transition zone. This occurs because grainsize evolution following spinel-to-post-spinel phase change and grain size dependent viscosity in Case 12 lead to dynamic formation of a weak layer beneath the phase boundary (Figures 3i and 3j). As the slab approaches the bottom of the mantle transition zone, some of the slab and its surrounding mantle materials undergo spinel-to-post-spinel phase change and sink into the lower mantle (Figures 3a and 3i). With the grainsize reduction for the post-spinel phase (i.e., by a factor of 30 as assumed in our models; Solomatov & Reese, 2008) (Figure 3e) and the grain size dependent viscosity, a weak zone is formed immediately below the phase boundary and slab (Figure 3i). As more upper mantle materials go into the lower mantle, the weak zone with reduced grainsize becomes broader and thicker (Figures 3j and 3f). The weak zone keeps the bulking slab in the mantle transition zone and moving horizontally, causing long deflected slab (Figure 3b), similar to how the prescribed weak layer in Cases 1 and 3 helps produce deflected slabs. At 42.8 Myr for Case 12, the horizontal length of the deflected slab in the mantle transition zone is slightly smaller than that in Case 1.

The size of the weak zone depends on two factors: mass flux from the upper mantle to the lower mantle and grain growth rate. In Case 12, the grainsize increases with time in the lower mantle (Equation 3) following the initial grainsize reduction after the phase change. Because the grain growth rate depends on both the temperature and grainsize, the grain growth rate is relatively small in the region with cold slab or at larger depth where the grainsize is larger after regrowth (Figures 3m and 3n). The larger the grain growth rate (e.g., the pre-factor K), the thinner the weak zone. Note that for Case 12 the weak zone forms preferentially below the subducting lithosphere (Figures 3i and 3j). This is determined by mantle downwelling which occurs below the subducting lithosphere (see flow velocities in Figures 3i and 3j). For Case 12 with relatively a small grain growth rate, the weak zone is sufficiently large to generate a significant deflected slab in the mantle transition zone.

Case 13 with a larger grain growth rate shows significantly shorter deflected slab in the mantle transition zone (Figure 3c) than that in Case 12 (Figures 3a–3b, Figures S3b and S5b). The larger grain growth rate in Case 13 (Figure 3o) causes the grainsize to increase more rapidly in the lower mantle, leading to significantly thinner and narrower weak zone (Figure 3k), compared with that of Case 12 (Figures 3i–3j). However, in the region where slab penetrates into the lower mantle, the weak layer is still thick due to the low temperature and small grain growth rate (Figures 3k, 3g and 3o). Without sufficiently large weak zone, Case 13 does not develop a significant deflected slab in the mantle transition zone.

While the grainsize reduction factor is fixed as 30 for Cases 12 and 13, this factor is not well constrained (e.g., Solomatov & Reese, 2008). We also performed calculations of Cases 14 and 15 that are identical to Cases 12 and 13 except the grainsize reduction factor is increased to 100 from 30. Larger grainsize reduction factor does not affect the results significantly as the grainsize could grow from $1/100$ to $1/30$ in a rather short time of less than 1 Myr (blue and red dashed lines in Figure S1b), because the grain growth rate is very large when the grainsize is small. While Case 14 shows long deflected slab as in Case 12 (Figure S5b), Case 15 with larger grainsize growth rate still does not develop significant deflected slab (Figures 3d, 3l, 3h and 3p and Figure S5b) as in Case 13.

The grain growth exponent m is strongly affected by the atomic diffusion mechanisms and could be greater than 3 (Fei et al., 2021; Solomatov et al., 2002; Yamazaki et al., 1996, 2009). We further computed Cases 16 to 23 with larger grain growth exponent m of 5.2 (Fei et al., 2021). Cases 16–19 are identical except their grain growth pre-exponent K are 10^2 , 10^3 , 10^4 , and 10^5 , respectively. Their grain size reduction factors are 3 (i.e., $c_{ph} = 1/30$; Table S2). Cases 16 with small grain growth rate also leads to long deflected slab at ~ 30 – 40 Myr. But the middle part of the slab in the mantle transition zone is not stable and sinks into the lower mantle at 42.4 Myr (Figure S6a) because of less reduction of viscosity in the weak zone compared with Case 12 (Figure 3j, Figure S6i, Equation 1). Cases 17, 18 and 19 with larger grain growth rates produce progressively less significant deflected slab, compared with that in Case 16, as expected (Figures S6b–S6d for Cases 17–19). Cases 20–23 are identical to Cases 16–19 except that the grainsize reduction factor is increased to

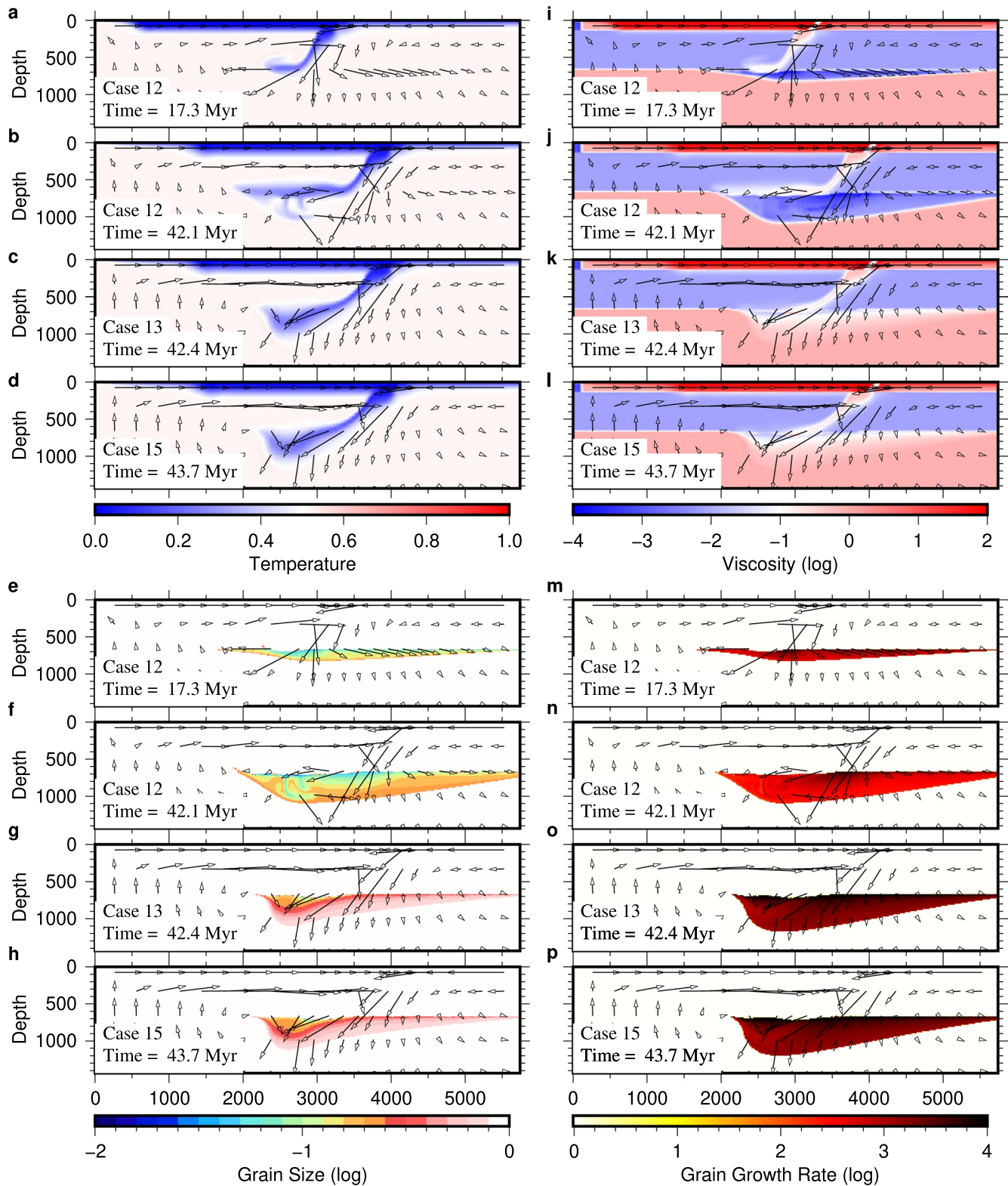


Figure 3. Snapshots of dimensionless temperature, viscosity, grain size and grain growth rate fields for Cases 12, 13 and 15. Cases 12 and 13 are identical except that their grainsize growth pre-exponent K are 10^3 and 10^5 , respectively. Case 15 is identical to Case 13 except the grainsize reduction factor increases to 100 instead of 30 in Case 13 (i.e., c_{ph} decreases from 1/30 to 1/100).

100 from 30. Case 20 shows similarly long deflected slab to that in Cases 12 and 16, while Cases 21–23 show similar results to Cases 17–19, respectively.

4. Discussions and Conclusions

While a number of mechanisms have been proposed to explain the seismically observed deflected slabs in the mantle transition zone, it has been a challenge to explain the long deflected slab in the western Pacific subduction zones for convection models using realistic Clapeyron slope of -2.0 MPa/K for the spinel-to-post-spinel phase change as suggested in laboratory experiments (Fei et al., 2004; Katsura et al., 2003; Litasov et al., 2005). Our 2-D models with a weak layer beneath the spinel-to-post-spinel phase transition and realistic Clapeyron slope successfully reproduce the long deflected slabs as observed in seismic models in the western Pacific, conforming previous 3-D global model results (Lourenço & Rudolph, 2020; Mao & Zhong, 2018). By implementing grain size dependent viscosity and grain size evolution for slabs going through spinel-to-post-spinel phase transition into the lower mantle, our models show that a dynamically generated weak layer could form below the phase boundary due to grain size effects and that the weak layer results in a long deflected slab in the transition zone. Our models also indicate that the geometry and viscosity reduction of the weak layer and the formation of deflected slab are strongly affected by the grain growth rate.

Our models show that a weak layer or zone beneath the spinel-to-post-spinel phase transition could cause a long deflected slab in the mantle transition zone (Figures 1a–1f and 1k–1n). The lubrication due to the weak layer beneath the slab is key in promoting the horizontal movement of the slab in the mantle transition zone and the formation of the long deflected slab. For the weak layer to be effective in producing long deflected slabs, it is important for the weak layer to occur beneath the slab as in previous 2-D regional (Grima et al., 2020) and 3-D global models (Lourenço & Rudolph, 2020; Mao & Zhong, 2018) and 2-D models here. Li et al. (2019) did not find the same effect of a weak layer as in our models, perhaps because the weak layer in their model was not placed directly beneath subducted slabs in the mantle transition zone. Our models also show that other factors, such as the trench retreat velocity and viscosity contrast between the upper and lower mantle, could also affect slab morphology significantly, which is consistent with previous studies (e.g., Zhong & Gurnis, 1995). While a large trench retreat velocity (e.g., Case 4 with $V_{tr} = 5$ cm/year; Figures 2a–2b) could also explain the deflected slab, which may be relevant to the Mariana subduction zone with its fast trench retreat and deflected slabs (e.g., Mao & Zhong, 2018), models without the weak layer could not explain the deflected slabs in subduction zones with a moderate trench retreat velocity (1–4 cm/year; Figure S4c) as in Japan subduction zones (Jolivet et al., 1994). Therefore, to understand the seismic observations of deflected slabs, it is crucial to consider realistic trench motion history as in 3D global mantle convection models with imposed plate motion history (Liu et al., 2021; Mao & Zhong, 2018, 2019). The viscosity contrast between the lower mantle and the upper mantle also plays an important role in the formation of deflected slab (Figures 2e–2h) and a viscosity contrast ratio larger than 30 is preferred for deflected slab formation. Slab strength does not appear to affect our model results significantly (Figures 2i–2l).

Our models with dynamically generated weak layer by considering grain size evolution indicates that the geometry and viscosity reduction of the weak layer due to spinel-to-post-spinel phase transition is strongly affected by the grain growth rate (Figure 3 and Figure S6). Due to low temperature of the subducted slab, the grain growth rate is significantly smaller within the slab than that in hot ambient mantle (Figures 3e–3h and Figures S6e–S6h). In general, the smaller the grain growth rate, the wider and thicker the weak layer and the stronger tendency to produce a long deflected slab in the mantle transition zone (Figure 3 and Figure S6). Neither the grain size reduction ratio nor the grain growth exponent in the lower mantle is well constrained (e.g., Solomatov & Reese, 2008). Recently, by conducting multi-anvil experiments for bridgmanite that coexists with ferropericlase, Fei et al. (2021) found a moderate grain growth exponent of 5.2 ± 0.3 , which is smaller than that of 10.6 ± 1.1 as reported by Yamazaki et al. (1996) but larger than that of 3–4 as suggested by Solomatov et al. (2002). If we scale the grain growth in Fei et al. (2021) using our normalization scheme, the corresponding dimensionless K is $\sim 1 \times 10^4$ (Figure S7), which is within the range of 10^3 – 10^5 as used in Cases 17–19 and 21–23. Note that Cases 17–18 and 21–22 produce deflected slab in the transition zone (Figures S6b–S6c for Cases 17–18). Therefore, our study provides a framework to quantitatively determine grain size evolution due to the phase change in the mantle that is poorly constrained. Future models with more detailed grain size evolution and dynamic trench evolution could further improve our understanding.

Data Availability Statement

Figures are drawn using the Generic Mapping Tools (GMT, www.soest.hawaii.edu/gmt/). The mantle convection code Citcom is available at <https://geodynamics.org/cig>. All model input parameters are given in Tables S1 and S2, and all data are available at <https://doi.org/10.6084/m9.figshare.14347358.v1>.

Acknowledgments

The authors are grateful to editor Steve Jacobsen and two anonymous reviewers for careful reviews of the paper. We also thank Hongzhan Fei for helpful discussions. This work is supported by National Science Foundation through grants 1645245 and 1940026. Our calculations were performed on supercomputers Cheyenne and RMACC Summit which are operated by the National Center for Atmospheric Research and University of Colorado at Boulder, respectively.

References

- Agrusta, R., Goes, S., & van Hunen, J. (2017). Subducting-slab transition-zone interaction: Stagnation, penetration and mode switches. *Earth and Planetary Science Letters*, *464*, 10–23. <https://doi.org/10.1016/j.epsl.2017.02.005>
- Behn, M. D., Hirth, G., & Elsenbeck, J. R., II (2009). Implications of grain size evolution on the seismic structure of the oceanic upper mantle. *Earth and Planetary Science Letters*, *282*(1–4), 178–189. <https://doi.org/10.1016/j.epsl.2009.03.014>
- Bellas, A., Zhong, S., Bercovici, D., & Mulyukova, E. (2018). Dynamic weakening with grain-damage and implications for slab detachment. *Physics of the Earth and Planetary Interiors*, *285*, 76–90. <https://doi.org/10.1016/j.pepi.2018.09.001>
- Bercovici, D., Mulyukova, E., & Long, M. D. (2019). A simple toy model for coupled retreat and detachment of subducting slabs. *Journal of Geodynamics*, *129*, 275–289. <https://doi.org/10.1016/j.jog.2018.03.002>
- Billen, M. I., Gurnis, M., & Simons, M. (2003). Multiscale dynamics of the Tonga-Kermadec subduction zone. *Geophysical Journal International*, *153*, 359–388. <https://doi.org/10.1046/j.1365-246x.2003.01915.x>
- Billen, M. I., & Hirth, G. (2007). Rheologic controls on slab dynamics. *Geochemistry, Geophysics, Geosystems*, *8*, Q08012. <https://doi.org/10.1029/2007GC001597>
- Christensen, U. R. (1996). The influence of trench migration on slab penetration into the lower mantle. *Earth and Planetary Science Letters*, *140*(1–4), 27–39. [https://doi.org/10.1016/0012-821x\(96\)00023-4](https://doi.org/10.1016/0012-821x(96)00023-4)
- Čížková, H., van Hunen, J., van den Berg, A. P., & Vlaar, N. J. (2002). The influence of rheological weakening and yield stress on the interaction of slabs with the 670 km discontinuity. *Earth and Planetary Science Letters*, *199*(3–4), 447–457.
- Dannberg, J., Eilon, Z., Faul, U., Gassmüller, R., Moulik, P., & Myhill, R. (2017). The importance of grain size to mantle dynamics and seismological observations. *Geochemistry, Geophysics, Geosystems*, *18*(8), 3034–3061. <https://doi.org/10.1002/2017gc006944>
- Fei, H., Faul, U., & Katsura, T. (2021). The grain growth kinetics of bridgmanite at the topmost lower mantle. *Earth and Planetary Science Letters*, *561*, 116820. <https://doi.org/10.1016/j.epsl.2021.116820>
- Fei, Y., Van Orman, J., Li, J., Van Westrenen, W., Sanloup, C., Minarik, W., et al. (2004). Experimentally determined postspinel transformation boundary in Mg₂SiO₄ using MgO as an internal pressure standard and its geophysical implications. *Journal of Geophysical Research*, *109*, B02305. <https://doi.org/10.1029/2003JB002562>
- French, S. W., & Romanowicz, B. A. (2014). Whole-mantle radially anisotropic shear velocity structure from spectral-element waveform tomography. *Geophysical Journal International*, *199*(3), 1303–1327. <https://doi.org/10.1093/gji/ggu334>
- French, S. W., & Romanowicz, B. A. (2015). Broad plumes rooted at the base of the Earth's mantle beneath major hotspots. *Nature*, *525*(7567), 95–99. <https://doi.org/10.1038/nature14876>
- Fukao, Y., & Obayashi, M. (2013). Subducted slabs stagnant above, penetrating through, and trapped below the 660 km discontinuity. *Journal of Geophysical Research*, *118*(11), 5920–5938. <https://doi.org/10.1002/2013jb010466>
- Garel, F., Goes, S., Davies, D. R., Davies, J. H., Kramer, S. C., & Wilson, C. R. (2014). Interaction of subducted slabs with the mantle transition-zone: A regime diagram from 2-D thermo-mechanical models with a mobile trench and an overriding plate. *Geochemistry, Geophysics, Geosystems*, *15*(5), 1739–1765. <https://doi.org/10.1002/2014gc005257>
- Glišović, P., Forte, A. M., & Ammann, M. W. (2015). Variations in grain size and viscosity based on vacancy diffusion in minerals, seismic tomography, and geodynamically inferred mantle rheology. *Geophysical Research Letters*, *42*, 6278–6286. <https://doi.org/10.1002/2015GL065142>
- Goes, S., Agrusta, R., Van Hunen, J., & Garel, F. (2017). Subduction-transition zone interaction: A review. *Geosphere*, *13*(3), 644–664. <https://doi.org/10.1130/GES01476.1>
- Grand, S. P., Van der Hilst, R. D., & Widiyantoro, S. (1997). High resolution global tomography: A snapshot of convection in the Earth. *Geological Society of America Today*, *7*(4), 1–7.
- Grima, A. G., Lithgow-Bertelloni, C., & Crameri, F. (2020). Orphaning regimes: The missing link between flattened and penetrating slab morphologies. *Frontiers in Earth Science*, *8*, 374. <https://doi.org/10.3389/feart.2020.00374>
- Hall, C. E., & Parmentier, E. M. (2003). Influence of grain size evolution on convective instability. *Geochemistry, Geophysics, Geosystems*, *4*(3), 1029. <https://doi.org/10.1029/2002GC000308>
- Holt, A. F., Becker, T. W., & Buffett, B. A. (2015). Trench migration and overriding plate stress in dynamic subduction models. *Geophysical Journal International*, *201*(1), 172–192. <https://doi.org/10.1093/gji/ggv011>
- Jolivet, L., Tamaki, K., & Fournier, M. (1994). Japan Sea, opening history and mechanism: A synthesis. *Journal of Geophysical Research*, *99*(B11), 22237–22259. <https://doi.org/10.1029/93jb03463>
- Karato, S. I. (2008). *Deformation of earth materials: An introduction to the rheology of solid earth*. Cambridge University Press.
- Katsura, T., Yamada, H., Shinmei, T., Kubo, A., Ono, S., Kanzaki, M., et al. (2003). Post-spinel transition in Mg₂SiO₄ determined by high P–T in situ X-ray diffractometry. *Physics of the Earth and Planetary Interiors*, *136*(1–2), 11–24. [https://doi.org/10.1016/s0031-9201\(03\)00019-0](https://doi.org/10.1016/s0031-9201(03)00019-0)
- King, S. D., Frost, D. J., & Rubie, D. C. (2015). Why cold slabs stagnate in the transition zone. *Geology*, *43*(3), 231–234. <https://doi.org/10.1130/g36320.1>
- Korenaga, J. (2005). Firm mantle plumes and the nature of the core–mantle boundary region. *Earth and Planetary Science Letters*, *232*(1–2), 29–37. <https://doi.org/10.1016/j.epsl.2005.01.016>
- Lee, C., & King, S. D. (2011). Dynamic buckling of subducting slabs reconciles geological and geophysical observations. *Earth and Planetary Science Letters*, *312*(3–4), 360–370. <https://doi.org/10.1016/j.epsl.2011.10.033>
- Li, Z. H., Gerya, T., & Connolly, J. A. (2019). Variability of subducting slab morphologies in the mantle transition zone: Insight from petrological-thermomechanical modeling. *Earth-Science Reviews*, *196*, 102874. <https://doi.org/10.1016/j.earscirev.2019.05.018>
- Litasov, K. D., Ohtani, E., Sano, A., Suzuki, A., & Funakoshi, K. (2005). Wet subduction versus cold subduction. *Geophysical Research Letters*, *32*, L13312. <https://doi.org/10.1029/2005GL022921>

- Liu, S., Ma, P., Zhang, B., & Gurnis, M. (2021). The Horizontal Slab beneath East Asia and Its Subdued Surface Dynamic Response. *Journal of Geophysical Research: Solid Earth*, 126, e2020JB021156. <https://doi.org/10.1029/2020jb021156>
- Lourenço, D. J., & Rudolph, M. L. (2020). Shallow lower mantle viscosity modulates the pattern of mantle structure. *Geochemistry, Geophysics, Geosystems*, 21, e2020GC008934. <https://doi.org/10.1029/2020GC008934>
- Mao, W., & Zhong, S. (2018). Slab stagnation due to a reduced viscosity layer beneath the mantle transition zone. *Nature Geoscience*, 11(11), 876–881. <https://doi.org/10.1038/s41561-018-0225-2>
- Mao, W., & Zhong, S. (2019). Controls on global mantle convective structures and their comparison with seismic models. *Journal of Geophysical Research*, 124(8), 9345–9372. <https://doi.org/10.1029/2019jb017918>
- Mao, W., & Zhong, S. (2021). Constraints on mantle viscosity from intermediate-wavelength geoid anomalies in mantle convection models with plate motion history. *Journal of Geophysical Research: Solid Earth*, 126(4), e2020JB021561. <https://doi.org/10.1029/2020jb021561>
- McNamara, A. K., & Zhong, S. (2004). The influence of thermochemical convection on the fixity of mantle plumes. *Earth and Planetary Science Letters*, 222(2), 485–500. <https://doi.org/10.1016/j.epsl.2004.03.008>
- Mitrovica, J. X., & Forte, A. M. (2004). A new inference of mantle viscosity based upon joint inversion of convection and glacial isostatic adjustment data. *Earth and Planetary Science Letters*, 225(1–2), 177–189. <https://doi.org/10.1016/j.epsl.2004.06.005>
- Moresi, L., & Gurnis, M. (1996). Constraints on the lateral strength of slabs from three-dimensional dynamic flow models. *Earth and Planetary Science Letters*, 138(1–4), 15–28. [https://doi.org/10.1016/0012-821x\(95\)00221-w](https://doi.org/10.1016/0012-821x(95)00221-w)
- Moresi, L., Zhong, S., & Gurnis, M. (1996). The accuracy of finite element solutions of Stokes's flow with strongly varying viscosity. *Physics of the Earth and Planetary Interiors*, 97(1–4), 83–94. [https://doi.org/10.1016/0031-9201\(96\)03163-9](https://doi.org/10.1016/0031-9201(96)03163-9)
- Panasjuk, S. V., & Hager, B. H. (1998). A model of transformational superplasticity in the upper mantle. *Geophysical Journal International*, 133(3), 741–755. <https://doi.org/10.1046/j.1365-246x.1998.00539.x>
- Ritsema, J., Deuss, A. A., Heijst, V., & Woodhouse, J. H. (2011). S40RTS: A degree-40 shear-velocity model for the mantle from new Rayleigh wave dispersion, teleseismic traveltimes and normal-mode splitting function measurements. *Geophysical Journal International*, 184(3), 1223–1236. <https://doi.org/10.1111/j.1365-246x.2010.04884.x>
- Rozel, A. (2012). Impact of grain size on the convection of terrestrial planets. *Geochemistry, Geophysics, Geosystems*, 13, Q10020. <https://doi.org/10.1029/2012GC004282>
- Rudolph, M. L., Moulik, P., & Lekić, V. (2020). Bayesian inference of mantle viscosity from whole-mantle density models. *Geochemistry, Geophysics, Geosystems*, 21(11), e2020GC009335. <https://doi.org/10.1029/2020gc009335>
- Seton, M., Müller, R. D., Zahirovic, S., Gaina, C., Torsvik, T., Shephard, G., et al. (2012). Global continental and ocean basin reconstructions since 200 Ma. *Earth-Science Reviews*, 113(3–4), 212–270. <https://doi.org/10.1016/j.earscirev.2012.03.002>
- Solomatov, V. S. (2001). Grain size-dependent viscosity convection and the thermal evolution of the Earth. *Earth and Planetary Science Letters*, 191(3–4), 203–212. [https://doi.org/10.1016/s0012-821x\(01\)00426-5](https://doi.org/10.1016/s0012-821x(01)00426-5)
- Solomatov, V. S., El-Khozondar, R., & Tikare, V. (2002). Grain size in the lower mantle: Constraints from numerical modeling of grain growth in two-phase systems. *Physics of the Earth and Planetary Interiors*, 129(3–4), 265–282. [https://doi.org/10.1016/s0031-9201\(01\)00295-3](https://doi.org/10.1016/s0031-9201(01)00295-3)
- Solomatov, V. S., & Reese, C. C. (2008). Grain size variations in the Earth's mantle and the evolution of primordial chemical heterogeneities. *Journal of Geophysical Research: Solid Earth*, 113, B07408. <https://doi.org/10.1029/2007JB005319>
- Stegman, D. R., Freeman, J., Schellart, W. P., Moresi, L., & May, D. (2006). Influence of trench width on subduction hinge retreat rates in 3-D models of slab rollback. *Geochemistry, Geophysics, Geosystems*, 7, Q03012. <https://doi.org/10.1029/2005GC001056>
- Thielmann, M., & Schmalholz, S. M. (2020). Contributions of grain damage, thermal weakening, and necking to slab detachment. *Frontiers in Earth Science*, 8, 254. <https://doi.org/10.3389/feart.2020.00254>
- van der Hilst, R. D., Widiyantoro, S., & Engdahl, E. R. (1997). Evidence for deep mantle circulation from global tomography. *Nature*, 386, 578–584. <https://doi.org/10.1038/386578a0>
- Wang, Y., & Li, M. (2020). Constraining mantle viscosity structure from a statistical analysis of slab stagnation events. *Geochemistry, Geophysics, Geosystems*, 21(11), e2020GC009286. <https://doi.org/10.1029/2020gc009286>
- Yamazaki, D., Kato, T., Ohtani, E., & Toriumi, M. (1996). Grain growth rates of MgSiO₃ perovskite and periclase under lower mantle conditions. *Science*, 274(5295), 2052–2054. <https://doi.org/10.1126/science.274.5295.2052>
- Yamazaki, D., Yoshino, T., Matsuzaki, T., Katsura, T., & Yoneda, A. (2009). Texture of (Mg, Fe) SiO₃ perovskite and ferro-periclase aggregate: Implications for rheology of the lower mantle. *Physics of the Earth and Planetary Interiors*, 174(1–4), 138–144. <https://doi.org/10.1016/j.pepi.2008.11.002>
- Yang, T., Moresi, L., Zhao, D., Sandiford, D., & Whittaker, J. (2018). Cenozoic lithospheric deformation in Northeast Asia and the rapidly-aging Pacific Plate. *Earth and Planetary Science Letters*, 492, 1–11. <https://doi.org/10.1016/j.epsl.2018.03.057>
- Zhong, S., & Davies, G. F. (1999). Effects of plate and slab viscosities on the geoid. *Earth and Planetary Science Letters*, 170(4), 487–496. [https://doi.org/10.1016/s0012-821x\(99\)00124-7](https://doi.org/10.1016/s0012-821x(99)00124-7)
- Zhong, S., & Gurnis, M. (1995). Mantle convection with plates and mobile, faulted plate margins. *Science*, 267(5199), 838–843. <https://doi.org/10.1126/science.267.5199.838>

References From the Supporting Information

- Christensen, U. R., & Yuen, D. A. (1985). Layered convection induced by phase transitions. *Journal of Geophysical Research*, 90(B12), 10291–10300. <https://doi.org/10.1029/jb090ib12p10291>
- Hager, B. H., & Richards, M. A. (1989). Long-wavelength variations in Earth's geoid: Physical models and dynamical implications. *Philosophical Transactions of the Royal Society A*, 328(1599), 309–327. <https://doi.org/10.1098/rsta.1989.0038>
- King, S. D. (1995). Radial models of mantle viscosity: Results from a genetic algorithm. *Geophysical Journal International*, 122(3), 725–734. <https://doi.org/10.1111/j.1365-246x.1995.tb06831.x>
- Turcotte, D. L., & Schubert, G. (2014). *Geodynamics*. Cambridge University Press.
- Zhong, S., & Gurnis, M. (1994). Role of plates and temperature-dependent viscosity in phase change dynamics. *Journal of Geophysical Research*, 99(B8), 15903–15917. <https://doi.org/10.1029/94jb00545>